Engineering Fracture Mechanics 275 (2022) 108825

Contents lists available at ScienceDirect

Engineering Fracture Mechanics

journal homepage: www.elsevier.com/locate/engfracmech

Mechanical and fatigue behaviour of polyamide 12 processed via injection moulding and selective laser sintering. Analysis based on Kitagawa-Takahashi diagrams

A. Salazar *, A.J. Cano, J. Rodríguez

DIMME, Grupo de Durabilidad e Integridad Mecánica de Materiales Estructurales, Universidad Rey Juan Carlos, C/ Tulipán, s/n, 28933 Móstoles, Madrid. Spain

ARTICLE INFO

Keywords:
Fatigue map
Fatigue limit
Long crack threshold
Polyamide 12
Selective Laser Sintering
Injection Moulding

ABSTRACT

This work deals with the mechanical and fatigue behaviour of polyamide 12 processed via Selective Laser Sintering and Injection Moulding. Apart from the analysis regarding the influence of the manufacturing technique, the effect of the layer orientation with respect to the direction of the applied load will be also analysed, since the additive manufacturing technique is a layer-wise technology that can induce anisotropy in the material. An extensive experimental program was carried out to determine the tensile, fracture, fatigue life and fatigue crack growth behaviours. The main novelty of this work lies, for the first time in polymers, in the use of the perspective of the Kitagawa-Takahashi diagrams for infinite fatigue life and by analogy their extension to failure.

1. Introduction

Failure diagrams are a powerful tool for safe design and safe use of structural components. In this sense, the Kitagawa-Takahashi diagram [1] constitutes a simple tool for design against fatigue as it combines the stress-based and the fracture mechanics methodologies in a safe-life approach (Fig. 1). It represents the stress level, $\Delta\sigma$, as a function of the crack or defect size, a, that will induce crack arrest. It establishes a lower bound for fatigue crack growth by gathering two limitating parameters, the fatigue endurance, $\Delta\sigma_f$, and the threshold for fatigue crack growth propagation, determined from precracked specimens, $\left(\Delta\sqrt{G}\right)_{th}$. $\Delta\sqrt{G}$ has been demonstrated to be more appropriate as crack driving force for polymers and composites than the stress intensity factor range, ΔK, due to the intrinsic viscoelastic behaviour of these materials and also when dealing with the R-ratio effect [2–6]. In this diagram, the threshold stress for crack propagation is represented as the minimum of either the stress-based approach.

$$\Delta\sigma \geq \Delta\sigma_f \tag{1}$$

or from the fracture mechanics.

$$\Delta\sigma \geq \frac{\left(\Delta\sqrt{G}\right)_{th}\sqrt{E^*}}{\sqrt{\pi a}} \tag{2}$$

* Corresponding author.
E-mail address: alicia.salazar@urjc.es (A. Salazar).

https://doi.org/10.1016/j.engfracmech.2022.108825
Received 8 June 2022; Received in revised form 13 September 2022; Accepted 19 September 2022
Available online 24 September 2022

where $E^* = E$ for plane stress conditions or $E^* = \frac{E}{1-\nu^2}$, with ν the Poissońs ratio, for plane strain state. In the first case, the initiation damage mechanism, controlled by the fatigue limit, can induce microstructurally small cracks (Microstructurally Short Crack, MSC, zone). In the second case, it is assumed that long cracks exist (Long Crack, LC, regime), and the fracture mechanics approach defines the conditions for crack arrest. The transition between these two regimes is governed by the Physically Short Crack zone (PSC), whose behaviour can be described neither by stress-based criteria nor by the fracture mechanics approach. As a result of fatigue failure occurring in the transition region, for values of the pair $(\Delta\sigma, a)$ below the lines of the Kitagawa-Takahashi diagram in which safe life is assumed, El Haddad et al. [7] proposed an empirical solution to match the asymptotic behaviour of the fatigue limit in the MSC zone with the threshold values of the LC regime through:

$$\frac{\Delta\sigma}{\Delta\sigma_f} = \sqrt{\frac{l_o}{a + l_o}} \tag{3}$$

where l_o is a characteristic crack length calculated as:

$$l_o = \frac{E^*}{\pi}\left(\frac{(\Delta\sqrt{G})_{th}}{\Delta\sigma_f}\right)^2 \tag{4}$$

Therefore, Eq. (3) defines a boundary (dotted line in Fig. 1), below which infinite fatigue life is predicted while above, a finite life should occur. Many studies have tried to identify the meaning of l_o [8–10], which is affected by microstructural features, the stress state and the testing conditions.

There are several authors (Larsen et al. [11], Ciavarella and Monno [12]) who have included in the Kitagawa-Takahashi diagrams the residual strength curves and information about the finite fatigue lifetime in what is known as the extended Kitagawa-Takahashi diagrams or generalized Kitagawa-Takahashi diagrams. The residual strength curves are constructed from the mechanical strength, as the tensile strength, σ_T, and the fracture toughness, K_{IC} or G_{IC}, obtained from plain and precracked specimens under quasistatic conditions, respectively. Meanwhile, the extended Kitagawa-Takahashi diagram for finite fatigue lifetime is computed from the S-N Basquin curve and the fatigue crack propagation law. In this way, it is possible to combine in a single representation the conditions to guarantee infinite fatigue life, finite life for a certain number of cycles and catastrophic failure, in a fatigue map.

The modified Kitagawa-Takahashi diagrams have been used for design under fatigue, fretting fatigue, stress corrosion and corrosion fatigue of metallic components [13–18], but the extent of this generalized Kitagawa-Takahashi diagrams to components made of polymers is unknown. Many may be the reasons. One has to do with the material itself. Polymers are viscoelastic and to obtain the characteristic fatigue parameters within the High Cycle Fatigue regime may be tough and very time consuming as normally the testing frequency must be very low [19]. Other has to do with the characterisation itself. Although there are some protocols and standards for the determination of the S-N curves [20] and the crack propagation law [19], there are uncertainties for the determination of the threshold parameters, fatigue limit and threshold for fatigue crack propagation, because there are no specific guidelines at all. Finally, and the most important, there is still some controversy regarding the crack driving force especially in the description of the

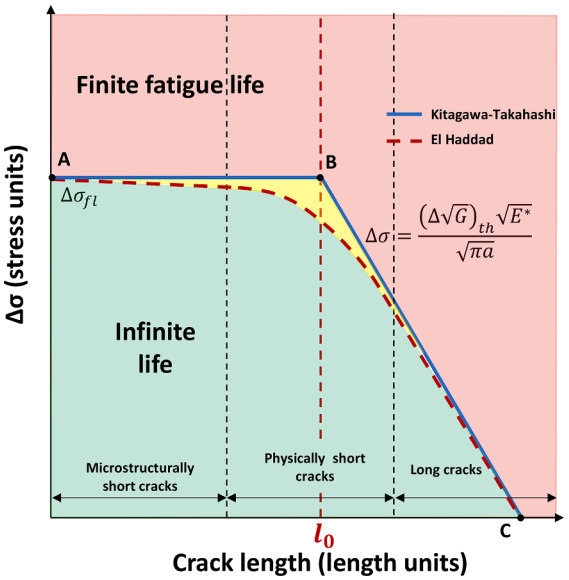

Fig. 1. Kitagawa-Takahashi diagram (continuous line in blue) with El Haddad approach (dotted line in red). The green area is the infinite fatigue lifetime zone, the red area is the finite fatigue lifetime region, and the yellow area is the area where approaches differ. Three zones are distinguished: microstructurally short crack (MSC), physically short crack (PSC) and long crack (LC) zones.

fatigue crack growth behaviour when dealing with the R-ratio effect [2–6]. Regarding this point, the use of $\Delta\sqrt{G}$ instead of ΔK has been previously explored by the authors [6].

Despite all these unsolved questions, there is a clear evidence, polymers are gaining more and more ground in different technological fields, increased even more in recent times with the advent of additive manufacturing (AM) techniques which allow larger design freedom. Selective Laser Sintering (SLS) stands out as an AM technique in which the mechanical properties of the polymeric parts are closely similar to those of parts fabricated using conventional techniques. Among the engineering thermoplastics, polyamide-based polymers, especially polyamide 12 (PA-12) are a very attractive for aeronautics, automotive and sports sectors because of its good impact resistance, excellent mechanical properties and high resistance to fatigue, coupled with a low cost. Nevertheless, these technologies cannot provide defect free PA-12 final products yet. The processing parameters, type of material and powder characteristics are important factors that play a key role in the surface roughness, dimensional accuracy, lack of fusion and pore structure and quantity, affecting the properties of the products including the mechanical properties [21–24]. Moreover, the resulting properties may result anisotropic as SLS is a layer-by-layer deposition technology [22–23].

In most of the applications in which SLS PA-12 can be employed, the design against fatigue is necessary and a fatigue map is essential for establishing reliable fatigue predictions. It is known to all that surface roughness and inherent defects are determining factors for fatigue performance. New and indirect methods capable of including the effect of flaws and of notches in the Kitagawa-Takahashi diagrams have been developed, extending those already initiated by Atzori and Lazzarin [14–15]. In this sense, it is worth mentioning the works of Ciavarella and Mono [12] in steels manufactured by conventional techniques, of Beretta and Romano [25] in AlSiMg and Ti-6Al-4 V alloys manufactured by AM and conventional processes and of Benedetti and Santus [26] in additively manufactured Ti-6Al-4 V alloy.

To the authors knowledge, all the works found in the literature regarding the discussion of the fatigue parameters in the light of the Kitagawa-Takahashi diagrams are focussed on metals processed via traditional or AM processes. Therefore, the objective of this paper is to determine a fatigue map through the extended Kitagawa-Takahashi diagrams of PA-12 fabricated via Injection Moulding (IM) and Selective Laser Sintering (SLS). As SLS can induce an anisotropic microstructure, the effect of the layered structure on the mechanical and fatigue parameters will be also analysed. It is worth mentioning that there is lack of information in the literature regarding the comparison of the mechanical and fatigue properties of IM and SLS PA-12. The authors have already published some results on the mechanical and fatigue data of SLS PA-12 [27–29]. In this work, new mechanical and fatigue data of IM PA-12 and new threshold values of fatigue crack growth propagation of SLS PA-12 are included, with the aim of building a complete fatigue diagram that allows comparisons between the materials manufactured by both techniques.

2. Experimental procedure

2.1. Materials

The material studied in this work is PA-12 manufactured via SLS and IM. For IM specimens, PA-12 Evonik Vestamid, supplied in form of pellets, was employed as raw material while for SLS samples, EOS PA2200 powder was used in an EOS Formiga P-100 LS machine with a CO_2 laser. The processing parameters are gathered in Table 1.

For the mechanical and fatigue characterisations of the SLS PA-12, two batches for each configuration were distinguished (Fig. 2). In those named as SLS 0°, the layered structure is disposed parallel to the applied force and in those named as SLS 90°, the layered structure is perpendicular to the applied force.

Prior to testing, some physical properties and microstructural features were quantified. The density was measured following the Archimedes methodology and using acetone as immersion medium. The surface roughness (roughness average, R_a, and average maximum height, R_z) was determined utilizing a roughness tester Mitutoyo SJ-301 equipped with a detector which the tip radius and angle were 60 μm and 60°, respectively. The microstructural parameter as the crystallinity degree, χ_C, was obtained through Differential Scanning Calorimetry (DSC) with a DSC Mettler 822e equipment. Specimens with 12.0 ± 0.5 mg in weight were firstly heated from 25 °C to 250 °C and subsequently cooled down from 250 °C to 25 °C at 10 °C/min. This process was performed twice in a row. Apart from the transition, melting and crystallization temperatures, the enthalpies were computed and used for the determination of the crystallinity degree. The microstructural characterisation was completed with the measurement of the spherulite size, $\overline{D}$. Films with thickness in the range between 3 and 15 μm were sectioned from the bulk using a rotatory microtome Leica RM2255 and inspected via optical microscopy using transmitted polarized light and dark field modes. More details for the determination of all these parameters can be found in [28–29].

Table 1
Manufacturing parameters of IM PA-12 and SLS PA-12.

IM					
Mould temperature	**Filling time**	**Holding time**	**Injection speed**	**Injection pressure**	**Mould clamping force**
60 °C	2.1 s	6.5 s	6–8 mm/s	10 MPa	1500 N
SLS					
Particle diameter	**Powder bed temperature**		**Frame temperature**	**Layer thickness**	**Laser power**
40–90 μm	171.5 °C		135.5 °C	0.2 mm	25 W

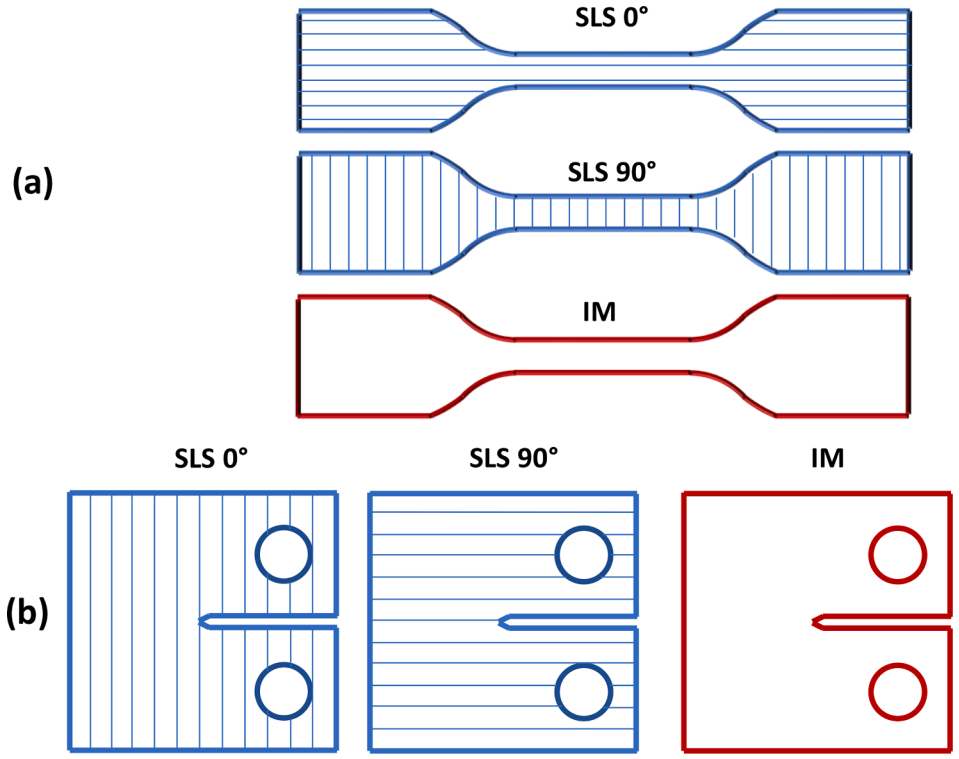

Fig. 2. Geometry of the specimens used in the experimental program where lines show layer orientation in SLS: (a) Dumbbell specimens for tensile and fatigue life tests. (b) Compact tension (CT) samples for fracture and fatigue crack growth tests.

2.2. Mechanical characterisation

Dumbbell specimens with nominal gage dimensions of 33 × 6 × 4 mm and 60 × 10 × 4 mm for SLS PA-12 and IM PA-12, respectively, were employed for the determination of the tensile properties following the guidelines of ASTM D638 [30] (Fig. 2a). The fracture parameters were determined through the ASTM E1820 recommendations [31] using the Compact Tension configuration (Fig. 2b) in specimens with 40 mm in width and 10 mm in thickness. A natural crack was inserted by tapping a razor blade frozen at liquid nitrogen temperature placed on the root of a machined notch of 16 mm in length. The final initial crack length, a_0, to width ratio was of 0.5. More information regarding the procedure and equipment can be consulted in [27].

2.3. Fatigue life tests

Fatigue tests were performed to obtain the S-N curve using the ASTM D 7791 standard [20] as a basis. The specimens had the same geometry (Fig. 2b) and dimensions as those used for the tensile characterisation. Tests were carried out at room temperature, at a frequency of 1 Hz, imposing a sinusoidal load wave under constant load amplitude at a stress ratio of 0.1. A servo-hydraulic testing machine MTS 810 Materials Testing was employed equipped with a load cell of ± 5 kN and a contact extensometer MTS 634.31F-24 (displacement range of + 4 mm/−2 mm) to measure the axial strain. The testing frequency was chosen so low to guarantee minimum temperature rise and avoid thermal fatigue. Twelve stress levels were analysed. The maximum stress of the cycle, σ_{max}, to the tensile strength ratio was between 58.75 % and 85 % to guarantee to be within the High Cycle Fatigue regime. At least, two repetitions for each stress level were performed. The results were fit to the Basquin equation:

$$\Delta\sigma = AN^b \tag{5}$$

with A and b materiaĺs coefficients.

The tests at the lowest values were stopped at 10^6 cycles due to the high-time consuming aspect, as the duration of the test without failure was of 11 days. Therefore, the tests with no failures after at 10^6 cycles were considered as run-outs. The estimation of the fatigue limit at 10^6 cycles was also pursued using the maximum likelihood method following a test sequence based on the staircase method. More details of this type of characterisation can be found in [29].

2.4. Fatigue crack growth tests

The fatigue crack growth behavior was described using as crack driving force $\Delta\sqrt{G}$, defined as:

$$\Delta\sqrt{G} = \sqrt{G_{max}} - \sqrt{G_{min}} \tag{6}$$

where G_{max} and G_{min} are the maximum and minimum energy release rates of the cycle, respectively. $\Delta\sqrt{G}$ is a valid similitude parameter for polymers as ΔK is for metals [5–6]. The crack growth rate, $\frac{da}{dN}$, versus $\Delta\sqrt{G}$ followed a Paris law type equation:

$$\frac{da}{dN} = C\left(\Delta\sqrt{G}\right)^n \tag{7}$$

with C and n materiaĺs constants. The configuration for this characterisation was Compact Tension (Fig. 2b), with the same dimensions as those employed for the fracture tests except for the machined notch length that was 8 mm. Also, the same notch sharpening procedure was followed to introduce the natural crack. The tests were performed following the recommendations of the ESIS TC4 protocol [19] and the ASTM E647 standard [32], with the aim of attaining the fatigue crack propagation curves and the crack propagation threshold values. Therefore, two procedures were followed, $\Delta\sqrt{G}$-increasing tests to determine the Paris law type parameters and $\Delta\sqrt{G}$-decreasing tests to achieve the threshold values. Between 5 and 10 tests were carried out per condition in increasing control parameter mode while 5 tests were performed per condition in decreasing control parameter.

The tests were carried out at room temperature, at a frequency of 1 Hz and a stress ratio of 0.1 imposing a sinusoidal load wave under constant load amplitude in a servo-hydraulic testing machine MTS 810 Materials Testing. A load cell of ± 5 kN and a crack opening displacement (COD) transducer MTS 632.02F-20 with a displacement range of + 3.9 mm/−2 mm were mounted on the testing machine. In the case of the $\Delta\sqrt{G}$-decreasing tests, a control parameter value below the critical values obtained from the fracture tests was initially applied in decreasing load amplitude mode using a normalized variation of the control parameter of $-0.05\ mm^{-1}$. The threshold values were achieved for crack growth rates down to $3{\cdot}10^{-7}$ mm/cycle. Two methods were used for obtaining the crack growth during the tests. In the first method, the crack growth was calculated by the compliance method using expressions determined for metals but also validated for polymers [19]. In addition, an optical method was used to validate the compliance method. Images were captured during the test at a specific frequency allowing the tracking of the crack length with a millimeter scale stuck to the specimen's surface. Moreover, the calculated final crack length was compared with the measured fatigue crack length on the fracture surface of each specimen. More details can be found in [28].

3. Results

3.1. Physical properties and microstructural analysis

Table 2 displays the physical properties and microstructural features of PA-12 as a function of the manufacturing process and of the orientation in SLS specimen. As observed, IM PA-12 density is higher than in SLS PA-12, with no differences between 0° and 90° orientations. Taking into account that full density of PA-12 is 1.02 g/cm^3, the porosity percentage was of 3.4 % for SLS and 0.2 % for IM materials, being the latter almost full dense. In case of the surface roughness, a clear difference is observed between SLS and IM materials, being the values of the former much higher than those of the latter. The high surface roughness of SLS specimens, together with a relative high porosity, is still an inherent weak point that can introduce uncertainties in the structural engineering design.

Regarding the microstructural analysis, PA-12 is a semicrystalline material being the crystalline phase in form of spherulites (Fig. 3). The crystallinity degree was 10 % higher in case of IM PA-12 but the size of the spherulites was four times smaller than that of SLS samples. Nevertheless, there is another microstructural characteristic in IM PA-12, the presence of a skin-core morphology with a skin layer size around 14 % of the total sample thickness (Fig. 4). The surface layer was completely amorphous and the spherulites were only observable in the core. The high molecular orientation occurring during the injection process together with the rapid cooling stage may create a high temperature gradient between the skin and the core resulting in a micro-spherulitic structure in the core and an amorphous outer layer.

3.2. Mechanical properties

Table 3 collects the mechanical properties obtained through tensile tests and the energy at crack growth initiation from fracture tests of IM PA-12 and SLS PA-12 at 0° and 90° orientations.

The results obtained in the tensile tests are in accordance with those found in the literature for SLS PA-12 [33] and IM PA-12 [34]. The main difference between SLS and IM specimens was in the elongation at break, with values twice or even 6 times higher depending on whether compared with SLS at 0° or at 90° orientation, respectively. Regarding the Youngś modulus and the tensile strength, the

Table 2
Density, ρ, porosity percentage, surface roughness parameters, R_z and R_a, crystallinity degree, χ_C, and spherulite size, $\overline{D}$, of IM PA-12 and SLS PA-12 at 0° and 90° orientations [28–29].

Orientation	ρ (g/cm^3)	Porosity (%)	R_a (μm)	R_z (μm)	χ_C (%)	$\overline{D}$ (μm)
IM	1.018 ± 0.005	0.19 ± 0.5	0.4 ± 0.2	3 ± 2	37.0 ± 0.2	13 ± 3
SLS 0°	0.982 ± 0.005	3.7 ± 0.5	12 ± 1	69 ± 8	33 ± 3	48 ± 12
SLS 90°	0.985 ± 0.005	3.4 ± 0.5	12 ± 4	60 ± 20	33 ± 3	49 ± 12

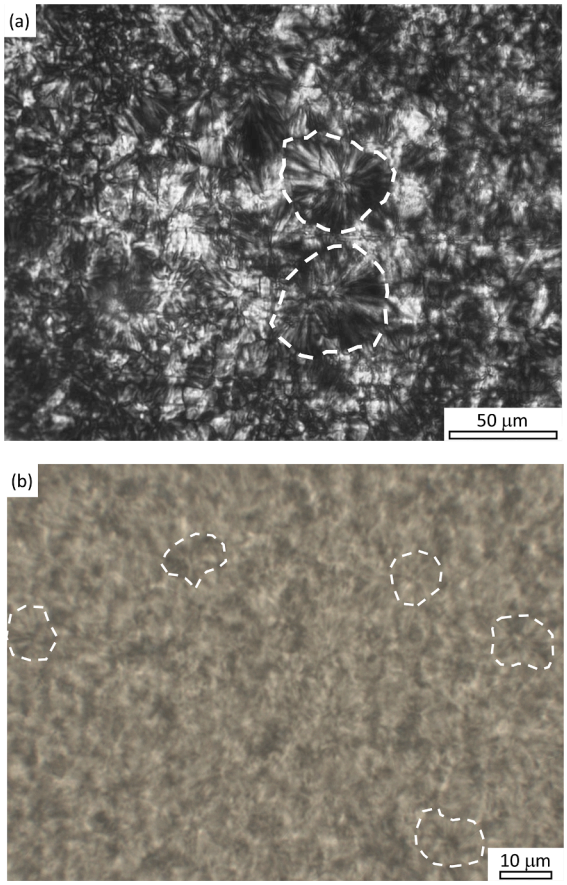

Fig. 3. Micrographs of (a) SLS PA-12 at 90° orientation [29] and (b) IM PA-12.

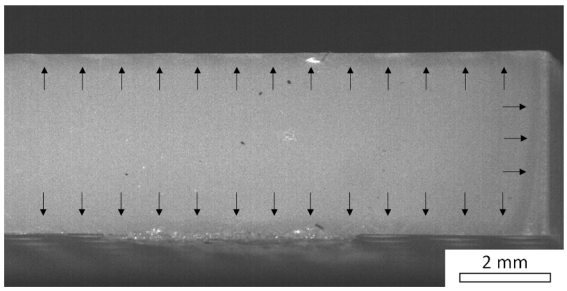

Fig. 4. Cross-section of IM PA-12 with a skin-core morphology where the skin is delimited by arrows.

Table 3
Tensile properties (Youngś modulus, E, Poissońs ratio, ν, tensile strength, σ_T, and elongation at break, ε_R) and fracture properties (energy at crack growth initiation J_{IC}) of SLS PA-12 at 0° and 90° orientations [27] and of IM PA-12.

	Tensile properties				Fracture properties
	E (GPa)	**ν**	**σ_T (MPa)**	**ε_R (%)**	**J_{IC} (kJ/m^2)**
IM	1.29 ± 0.04	0.46 ± 0.02	41 ± 1	64 ± 3	8.1 ± 1.2
SLS 0°	1.64 ± 0.03	0.43 ± 0.02	47 ± 1	27 ± 2	7.0 ± 0.6
SLS 90°	1.58 ± 0.04	0.41 ± 0.01	44 ± 2	10 ± 4	6.7 ± 1.2

values obtained in IM samples were smaller than in SLS samples, with differences of 27 % and 15 %, respectively. This can be striking considering that IM specimens were almost full dense, and their crystalline degree was 10 % higher than in SLS samples. Nevertheless, these initially contradictory results can be explained in the light of the presence of an amorphous skin in IM samples, a different thermal history during the manufacturing processes and the use of starting powders and pellets supplied by different providers. The latter indicative that it may not be the same material. Concerning the energy at crack growth initiation, the values of IM PA-12 were the highest, with differences of 20 %. Finally, when comparing the two orientations in SLS specimens, the main difference is again in the elongation at break with rare differences in the rest of parameters.

3.3. Fatigue life properties

The S-N fatigue curves for SLS PA-12 at 0° and 90° orientations can be found in [29]. Nevertheless, this section is focused on showing the difference between SLS and IM curves. Fig. 5 shows the fatigue lifetime curves obtained at a frequency of 1 Hz and a stress ratio of 0.1 of IM PA-12 and SLS PA-12 at 0° and 90° orientations, considering run-outs those tests which reached 10^6 cycles (duration of 11 days) without failure. Table 4 shows the Basquin parameters (Eq. (5)) together with the fatigue limit at 10^6 cycles, $\Delta\sigma_{fl}$ [29].

The fatigue performance is very similar regardless of the processing technique, but some differences are noteworthy. The exponent b of the Basquin law in IM samples was almost one half that of the SLS specimens. Regarding the orientation in SLS samples, the performance was better at 0° orientation with almost the same exponent value [29]. Finally, concerning the fatigue limit, IM samples presented the highest value and SLS at 90° orientation the lowest.

3.4. Fatigue crack growth behavior

The fatigue crack growth parameters of IM and SLS specimens are shown in Table 5. From the $\Delta\sqrt{G}$-decreasing tests, the threshold value $\left(\Delta\sqrt{G}\right)_{th}$ is displayed, meanwhile from the $\Delta\sqrt{G}$-increasing tests, the coefficients from the Paris law type equation (Eq. (7)), C and n, the maximum values of the crack driving force of the last cycle before catastrophic failure, $\left(\sqrt{G}\right)_{max}$, and the square root of the energy at crack growth initiation, $\sqrt{J_{IC}}$, are collected.

With the aim of facilitating the analysis, Fig. 6 gathers in one single graph the fatigue crack propagation behavior of IM PA-12 and SLS PA-12 at 0° and 90° orientations, with the characteristic dispersion represented with a shaded area which envelopes all the fatigue crack propagation curves of each material and condition. As in case of the fatigue life properties, the fatigue crack growth behavior is very similar independently of the manufacturing technique and the orientation in SLS samples, but some points are worth mentioning. Firstly, regarding the manufacturing technique, the fatigue crack growth behavior of IM PA-12 is in between those of SLS PA-12 at 0° and 90° orientations, with the smallest threshold values but with the steepness of the Paris law curve similar to that of SLS PA-12 at 0° orientation. Secondly, concerning the orientation, the best performance was attained at 0° orientation and the worst at 90° orientation as extensively discussed in [28]. Thirdly, the maximum values of the crack driving force of the last cycle before rupture are identical to the square root of the energy at crack growth initiation.

When comparing these data with those obtained in the literature, there is hardly works analyzing the influence of the manufacturing technique, except that of Blattmeier et al. [35] and Boukhili et al. [36]. Both works considered ΔK as the crack driving

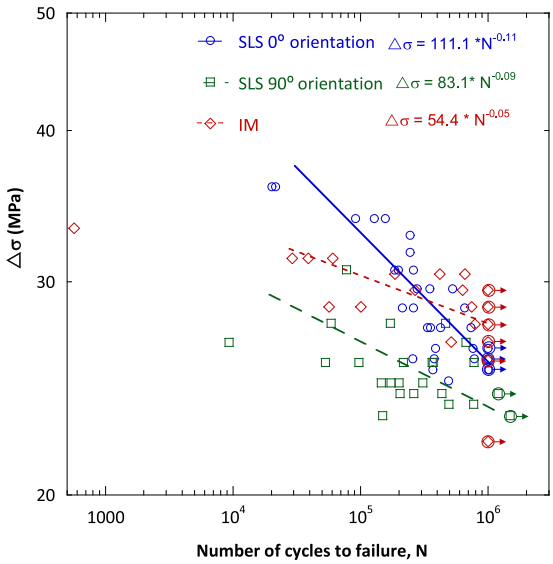

Fig. 5. S-N fatigue life curves of SLS PA-12 at 0° and 90° orientations [29] and of IM PA-12. ○ represents the run-outs after 10^6 cycles.

Table 4
Basquin law ($\Delta\sigma = AN^b$) coefficients and fatigue limit at 10^6 cycles, $\Delta\sigma_{fl}$, of SLS PA-12 at 0° and 90° orientations [29] and of IM PA-12.

	Basquin law		$\Delta\sigma_{fl}$ (MPa)
	A	b	
IM	54.4	−0.05	28 ± 1
SLS 0°	111.1	−0.11	26 ± 1
SLS 90°	83.1	−0.09	23 ± 1

Table 5
Fatigue parameters of SLS PA-12 at 0° and 90° orientations [28] and IM PA-12. From $\Delta\sqrt{G}$-decreasing tests, threshold values of the control parameter $(\Delta\sqrt{G})_{th}^{*}$. From $\Delta\sqrt{G}$-increasing tests average values of C and n parameters from Paris law (eq. (1)), maximum value of the crack driving force before break, $(\sqrt{G})_{max,c}$. Square root of the energy at crack growth initiation $\sqrt{J_{IC}}$.

	$\Delta\sqrt{G}$-decreasing	$\Delta\sqrt{G}$-increasing			Fracture tests
	$(\Delta\sqrt{G})_{th}^{*}$ (kJ/m^2)$^{1/2}$	C	n	$(\sqrt{G})_{max}$ (kJ/m^2)$^{1/2}$	$\sqrt{J_{IC}}$ (kJ/m^2)$^{1/2}$
IM	1.0 ± 0.2	$5{\cdot}10^{-6}$	9.0 ± 0.5	3.0 ± 0.3	2.8 ± 0.2
SLS 0°	1.3 ± 0.1	$6{\cdot}10^{-6}$	9 ± 2	2.6 ± 0.2	2.6 ± 0.1
SLS 90°	1.1 ± 0.2	$10{\cdot}10^{-6}$	10 ± 2	2.5 ± 0.3	2.6 ± 0.2

*Computed at crack growth rate downs to $3{\cdot}10^{-7}$ mm/cycle.

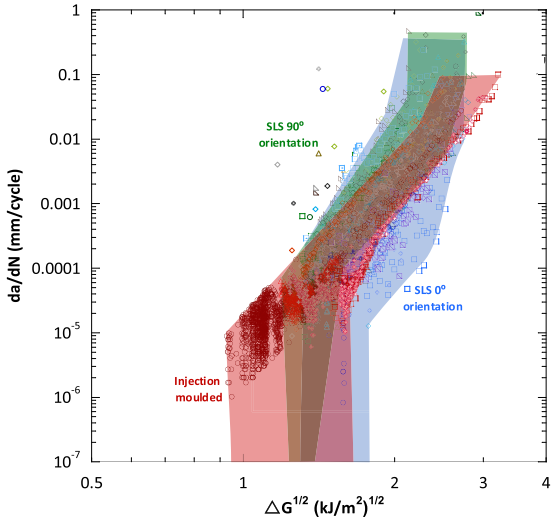

Fig. 6. Fatigue crack growth behavior comparison of PA-12 manufactured by IM (in red) and by SLS at 0° orientation (in blue) and at 90° orientation (in green) [28].

force. Blattmeir et al. [35] observed a clear worse behavior of IM PA-12 in comparison with that of SLS PA-12 and no influence of the orientation in SLS samples. And Boukhili et al. [36] concluded that ΔK was not an adequate parameter for the description of the fatigue crack propagation behavior of PA-12. In none of these works there are fittings of the experimental data to the Paris law equation and the data reported by Blattmeier et al. [35] were not attained at constant load amplitude.

3.5. Fractographic analysis

Figs. 7 and 8 display the fracture morphology of the tests performed on plain and precracked samples of SLS PA-12 at 0° orientation and of IM PA-12, respectively. The plain specimens were employed for the determination of the tensile and fatigue life properties and the precracked samples for the assessment of the fracture and fatigue crack growth behaviours. The micromechanism of failure of SLS PA-12 was the same for all the testing configurations and corresponded with the nucleation, growth and coalescence of crazes [37–38]. This phenomenon is characterised by fracture surfaces with a patchwork pattern (Fig. 7), that is, populated with voids surrounded by stretched amorphous filaments of PA-12, finally broken following the crack growth direction.

In the IM PA-12 fracture surfaces, it is necessary to differentiate between the morphologies of the fracture surfaces obtained in tests

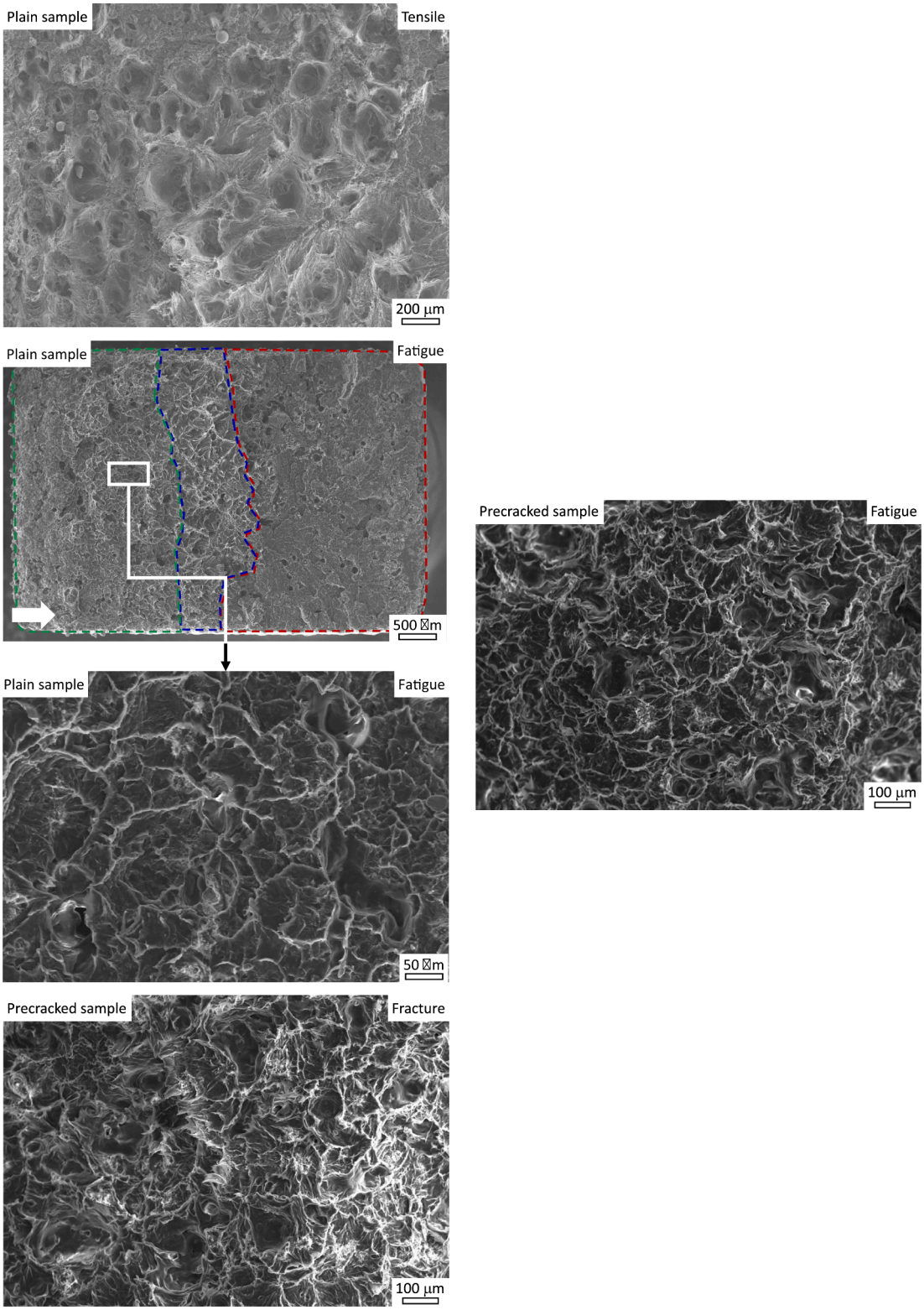

Fig. 7. Fractography of SLS PA-12 at 0° orientation: fracture surfaces obtained from plain samples employed for tensile [27] and fatigue life [29] (panoramic and detailed views) characterisations; fracture surfaces obtained from precracked samples used for fracture [27] and fatigue crack growth [28] characterisations.

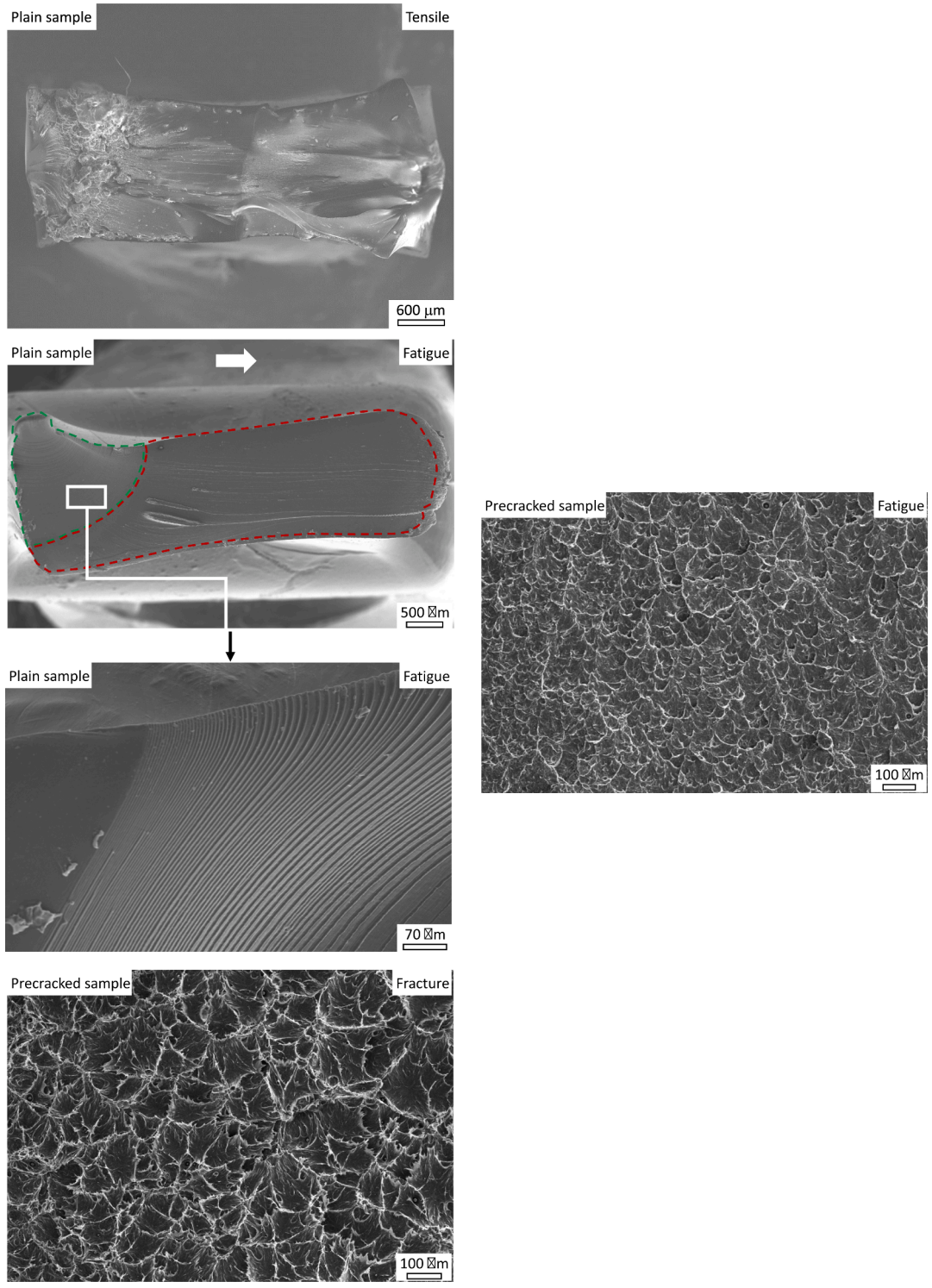

Fig. 8. Fractography of IM PA-12: fracture surfaces obtained from plain samples employed for tensile and fatigue life (panoramic and detailed views) characterisations; fracture surfaces obtained from precracked samples used for fracture and fatigue crack growth characterisations.

carried out on plain and on precracked specimens (Fig. 8). The fractography of the broken pieces obtained from tests performed on plain samples evidenced ductile tearing predominance with an evident starting defect at the surface (Fig. 8 plain samples). Therefore, the presence of an amorphous skin zone seems to prevail in the development of this different micromechanism of failure in comparison

with SLS specimens. On the other hand, the fracture surfaces obtained from tests carried out on precracked samples presented similar morphology to that of SLS samples, that is, a patchwork pattern (Fig. 8 precracked samples). Therefore, the failure mechanism was the nucleation, growth and coalescence of crazes, giving rise to dimples surrounded of stretched filaments. Nevertheless, in SLS specimens, the patchy surface seems to be grosser than in IM samples. The finer size of the patch in the IM samples could be related to the small size of the crystalline structure, together with the lack of processing defects, providing higher values of the fracture toughness [39] and larger values of the elongation at break (Table 3).

It is worth pointing out that the fracture surfaces obtained from the fatigue life tests presented three different zones in SLS PA-12 (Fig. 7 plain samples – fatigue – panoramic view): the subcritical crack growth area (outlined in green), the transition region (delimited in blue) and the unstable crack growth zone (outlined in red) [29]. Nevertheless, in IM PA-12 only two zones were distinguishable corresponding to the subcritical crack growth zone (outlined in green) and the unstable crack propagation region (bordered in red) (Fig. 8 plain samples – fatigue - panoramic view). In all cases, the crack initiation occurred at some point at the surface, promoted by the high surface roughness in SLS PA-12 or by a defect belonging to the skin layer due to the presence of small sink marks in IM PA-12. The inspection of the subcritical crack growth region revealed the different micromechanisms of failure. While in SLS PA-12 samples,

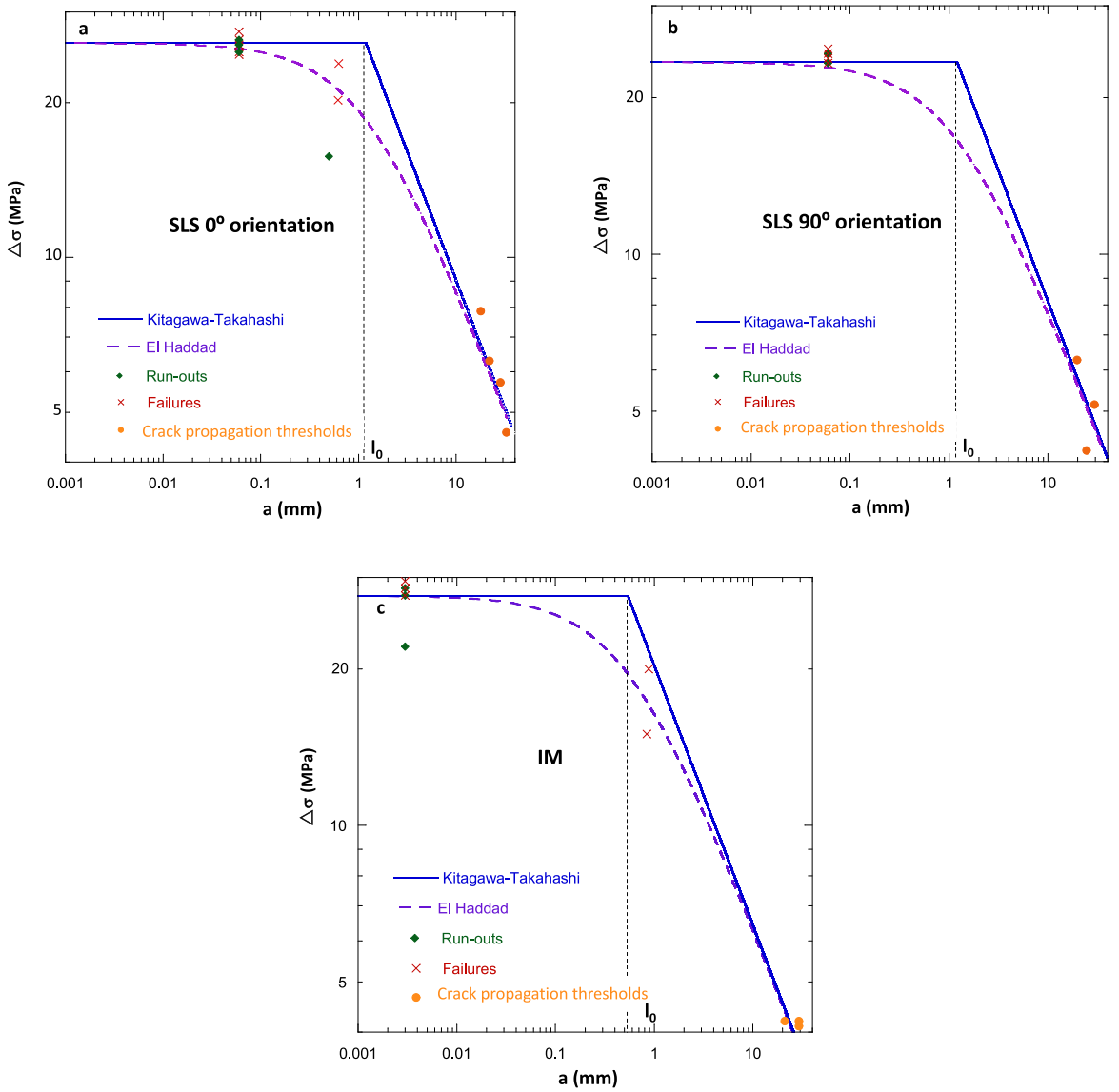

Fig. 9. Kitagawa-Takahashi diagram (continuous blue line) with El Haddad empirical model (dotted purple line) of (a) SLS PA-12 at 0° orientation, (b) SLS PA-12 at 90° orientation and (a) IM PA-12. The crack propagation thresholds, from $\Delta\sqrt{G}$-decreasing tests, are plotted with orange circles; run-outs and failures, from the tests employed for the fatigue limit determinations, are plotted as diamonds and crosses, respectively. Tests in the PSC zone are also included.

the patchy irregular surface revealed that crazing was the dominant mechanism of failure [29] (Fig. 7 plain samples – fatigue – detailed view), in IM PA-12, macroductile tearing with strong reduction of the gage length and a fracture surface populated by fatigue striations bowing out in the direction crack growth induced the fatigue failure (Fig. 8 plain samples fatigue – detailed view). Moreover, the spacing of the fatigue striations became larger as moving away from the surface defect responsible of the crack nucleation.

Summing up, the environment surrounding the crack initiation nuclei governs the mechanism of deformation and fracture. If crystalline phase populates the surroundings, the resulting mechanism of failure is crazing. Otherwise, ductile tearing occurs as in case of the IM samples.

Finally, there were hardly differences between the fracture surfaces of the two orientations in SLS samples, except for low level of deformation of the amorphous filaments undergone by the SLS PA-12 at 90° orientation [27–29].

4. Discussion

The experimental program detailed in the previous section is just the starting point for a discussion from a more global perspective based on the Kitagawa-Takahashi diagrams. Three aspects of the fracture and fatigue behavior are to be considered: "infinite" fatigue life, finite fatigue life and static residual strength, ending up in a fatigue map including all the possible scenarios. It is important to mention that in this work "infinite" fatigue life behavior has been assumed for 10^6 cycles without causing failure in plain samples. The reason of establishing the fatigue limit at that number of cycles is related with the low frequency chosen in this research, of 1 Hz, to avoid thermal interactions.

4.1. *"Infinite" fatigue life*

The Kitagawa-Takahashi diagrams including the predictions of El Haddad approach have been constructed using Eqs. (2) and (3) with the threshold of the crack driving force describing the fatigue crack propagation, $\left(\Delta\sqrt{G}\right)_{th}$, obtained from precracked samples, and with the fatigue limit at 10^6 cycles, $\Delta\sigma_{fl}$, determined from plain samples.

Fig. 9 shows the Kitagawa Takahashi diagrams (continuous line) with El Haddad curves (dotted line) of SLS PA-12 at 0° and 90° orientations and of IM PA-12. Experimental data from the tests employed for the determination of the fatigue limit and from $\Delta\sqrt{G}$-decreasing tests were included. A defect size equal to the surface roughness (Table 2) was assigned to the former, describing the run-outs with diamonds and the failure with crosses. Meanwhile the tests used for attaining the threshold of precracked samples were displayed with filled orange circles. Moreover, for SLS PA-12 at 0° orientation and IM PA-12, fatigue tests on dumbbell specimens with short cracks have been also included with the aim of assessing experimentally the PSC regime. The short cracks were introduced in the dumbbell specimens employed for the determination of the fatigue lifetime behavior via pressing a microtome razor blade with a tip diameter of 5.3 μm, ensuring a crack tip radius around 10 μm, which is below the estimated limit for considering the crack as a natural crack in polymers [40]. After introducing the sharp crack, the crack front was inspected via optical means to guarantee no damage in form of microcracks or whitening. Otherwise, the samples were discarded. The procedure for short crack introduction in SLS 90° orientation resulted unfruitfully as all specimens broke into two pieces when inserting the razor blade as a crack propagated unstably along the layeŕs interface. As observed, the experimental points attained in the PSC regime fit well to El Haddad model.

From the intersection of the MSC and the LC regimes in the Kitagawa Takahashi diagrams, a characteristic length, l_o, is obtained and shown in Table 6. This length can be interpreted as the limiting dimension of a subcritical defect above which the control parameter changes from $\Delta\sigma_{fl}$ to $\left(\Delta\sqrt{G}\right)_{th}$. As observed in Table 6, l_o of IM PA-12 is much smaller than those of SLS PA-12, with no differences between the distinct orientations in SLS. The behavior in the different regimes of the materials under study can be more easily evaluated through Fig. 10, in which IM PA-12 is the most resistant in the MSC regime while the best performance in the LC zone is attained by SLS at 0° orientation followed by SLS at 90° orientation. The explanation could be found in the defects introduced during the manufacturing process and in the microstructural features. The reason of the better performance of IM PA-12 at MSC zone could be accounted by the lack of defects in form of pores and unmolten particles, typical defects appearing in SLS samples that act in detriment of the fatigue limit (Table 4). On the other hand, when long cracks are present in SLS, the manufacturing defects go into the background and the spherulites probably come to play a key role. In SLS specimens, the spherulite size was 4 times higher than in IM samples (Table 2), with the consequent higher values of the threshold crack propagation parameter of the former.

Fig. 11 displays the normalized diagrams constructed by normalizing the stress range by the fatigue limit at 10^6 cycles for each material and the crack length by the characteristic length, including also the experimental data. As observed, El Haddad model predictions are more accurate than those of Kitagawa Takahashi, but some discrepancies are especially important in the PSC regime for IM PA-12 because some failures fall within the integrity zone.

Table 6
Characteristic length, l_o, of the materials under study.

	l_o (mm)
SLS 0°	1.2
SLS 90°	1.21
IM	0.54

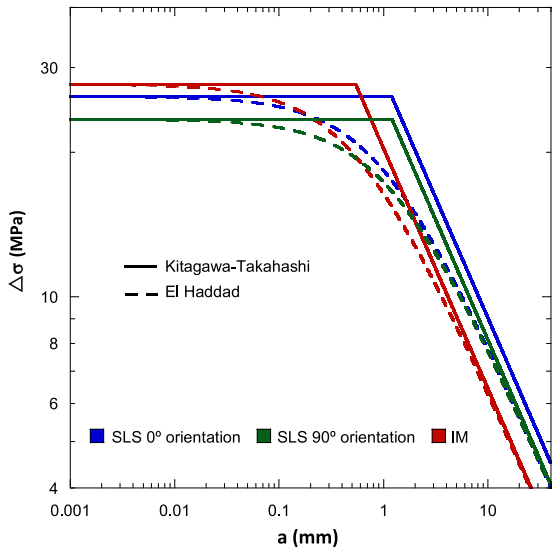

Fig. 10. Kitagawa-Takahashi diagrams (continuous line) and El Haddad empirical models (dotted line) of IM PA-12 (in red), SLS PA-12 at 0° orientation (in blue) and SLS PA-12 at 90° orientation (in green).

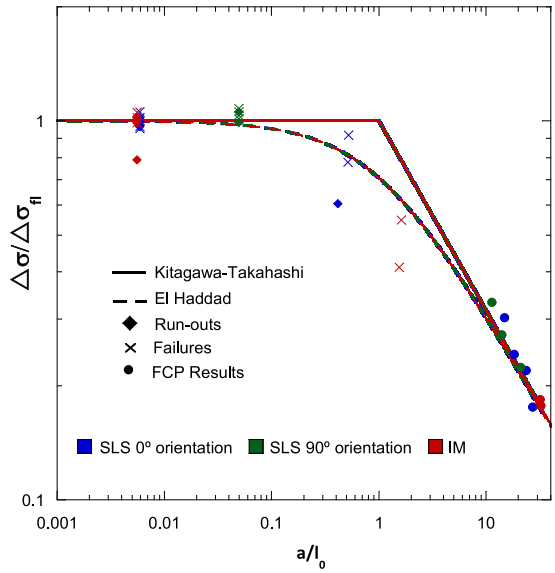

Fig. 11. Normalized Kitagawa-Takahashi diagrams (continuous line) and El Haddad empirical models (dotted line) of IM PA-12 (in red), SLS PA-12 at 0° orientation (in blue) and SLS PA-12 at 90° orientation (in green).

4.2. Residual strength diagrams

Kitagawa-Takahashi diagram can be extended to static failure occurring at one half cycle. The tensile strength, σ_T, obtained from tests on plain samples is employed for the characterisation of the MSC regime while the fracture toughness, G_{IC}, determined through precracked specimens is used for computing the nominal strength that characterises the LC zone through:

$$\sigma = \frac{\sqrt{E^* G_{IC}}}{\sqrt{\pi a}} \tag{8}$$

El Haddad approach can be also employed for static loading introducing a static characteristic length, l_0^s, computed as:

$$\frac{\sigma}{\sigma_T} = \sqrt{\frac{l_0^s}{a + l_0^s}} \tag{9}$$

with

$$l_0^s = \frac{1}{\pi}\frac{E^* G_{IC}}{\sigma_T^2} \tag{10}$$

Fig. 12 displays the residual strength diagrams based on the Kitagawa-Takahashi representation in continuous line and the modified El Haddad approach in dotted line of SLS PA-12 at 0° and 90° orientations and of IM PA-12. Experimental data used for the determination of the tensile and of the fracture parameters are also included. In addition, the tests realized in specimens with small and medium cracks size lengths in the range between 0.2 mm and 3 mm for IM PA-12 and SLS PA-12 at 0° orientation are also plotted.

The comparison of the static response can be analysed more easily in Fig. 13 which collects the residual strength curves of the three materials. The best performance in the MSC zone is that of the SLS PA-12 at 0° orientation with hardly differences among the three materials in the LC regime. The static characteristic length of IM PA-12 is much larger than that of SLS PA-12, with again scarce differences between the orientation in SLS specimens (Table 7). When comparing these values with the values of the characteristic length under "infinite" fatigue life (Table 6), the static values are much larger than those under "infinite" fatigue life, which is expected taking into account the values of the parameters employed for the determination (Eq. (10) and Table 3). These differences were of 25 % in SLS PA-12 but up to 300 % in IM PA-12.

Fig. 14 displays the normalized residual strength diagrams obtained by normalizing the nominal stress by the tensile strength and the crack length by the static characteristic length. Again, the predictions of El Haddad model are more accurate than those of Kitagawa-Takahashi predictions in the PSC zone but even this model can provide conservative predictions in case of IM PA-12.

4.3. Finite fatigue lifetime

Fig. 15 shows the extended Kitagawa-Takahashi and El Haddad diagrams where the static bearing capacities, the "infinite" fatigue lifetime (non-fatigue failure at 10^6 cycles assumed as infinite) and the finite lifetime information are included for SLS PA-12 at 0° orientation in blue, SLS PA-12 at 90° orientation in green and IM PA-12 in red. The upper boundary corresponds to the static conditions while the lower boundary relates to the "infinite" fatigue lifetime. Between these two frontiers, in the LC regime, all the experimental fatigue crack growth curves obtained from the $\Delta\sqrt{G}$-increasing tests have been also displayed. These curves fell within the region that started close to the fatigue limit boundary of each material, ending up at the boundary of stable crack propagation defined at static loading.

The finite fatigue lifetime band, defined as the tensile strength to fatigue limit ratio in the MSC zone, and the fracture toughness to the threshold for long cracks in the LC regime, has different size depending on the manufacturing process. The band in the MSC regime maintains constant in size independently of the orientation in the SLS PA-12 samples but it is clearly reduced in IM PA-12. This tendency may be supported by the fact that the band size is related to the population of defects, which is larger in SLS than in IM samples and consequently, the size of the former is bigger than of the latter. This contrasts with the behavior in metals, in which the band in the MSC zone holds constant independently of the microstructure [41]. On the other side, the band in the LC regime was larger for IM PA-12 than for SLS PA-12, with hardly differences in size between the distinct orientations. In metals, the fracture toughness to threshold stress intensity factor is related to microstructure [31] as well as in polymers, where the fracture toughness is also dependent on the spherulite size [35,39]. The higher the spherulite size, the lower the fracture parameters. This is the case for the materials under study (Tables 2 and 3). Regarding the threshold fatigue crack growth parameter, this could be also related to the crystalline phase, but further investigation is required in this topic because the link and type of dependency is still uncertain.

5. Conclusions

This work has analysed the mechanical and fatigue behaviour of polyamide 12 processed via the additive manufacturing technique as Selective Laser Sintering and the conventional technique as Injection Moulding. As SLS is a layer-wise technology, the characterisation was carried out applying the load parallel and perpendicularly to the layered structure.

The processing technique influenced the resulting physical properties and microstructure. IM samples were full dense, with a skin-core morphology in which the skin was completely amorphous, and the crystallinity degree was 10 % higher than that of SLS samples. On the other hand, the spherulite size was 4 times smaller. In case of the mechanical properties, IM samples presented the highest elongation at break and fracture toughness, and in the Selective Laser Sintering specimens, the elongation at break of the samples with the load applied parallel to the layered structure was larger than when the load was applied perpendicularly.

The fatigue behaviour evaluated at room temperature at a stress ratio of 0.1 and a frequency of 1 Hz was similar independently of the orientation and manufacturing technique. Nevertheless, SLS PA-12 at 0° orientation presented the best fatigue performance of either plain or precracked samples, SLS PA-12 at 90° orientation the worst and IM PA-12 an intermediate behaviour. IM PA-12 showed the highest fatigue limit at 10^6 cycles and the lowest long crack threshold. In SLS, samples at 0° orientation exhibited higher fatigue limit and long crack threshold values than at 90° orientation. The presence of defects play an important role in the characterisation with plain samples while the microstructural features as the spherulites govern the behaviour in the characterisation with precracked specimens.

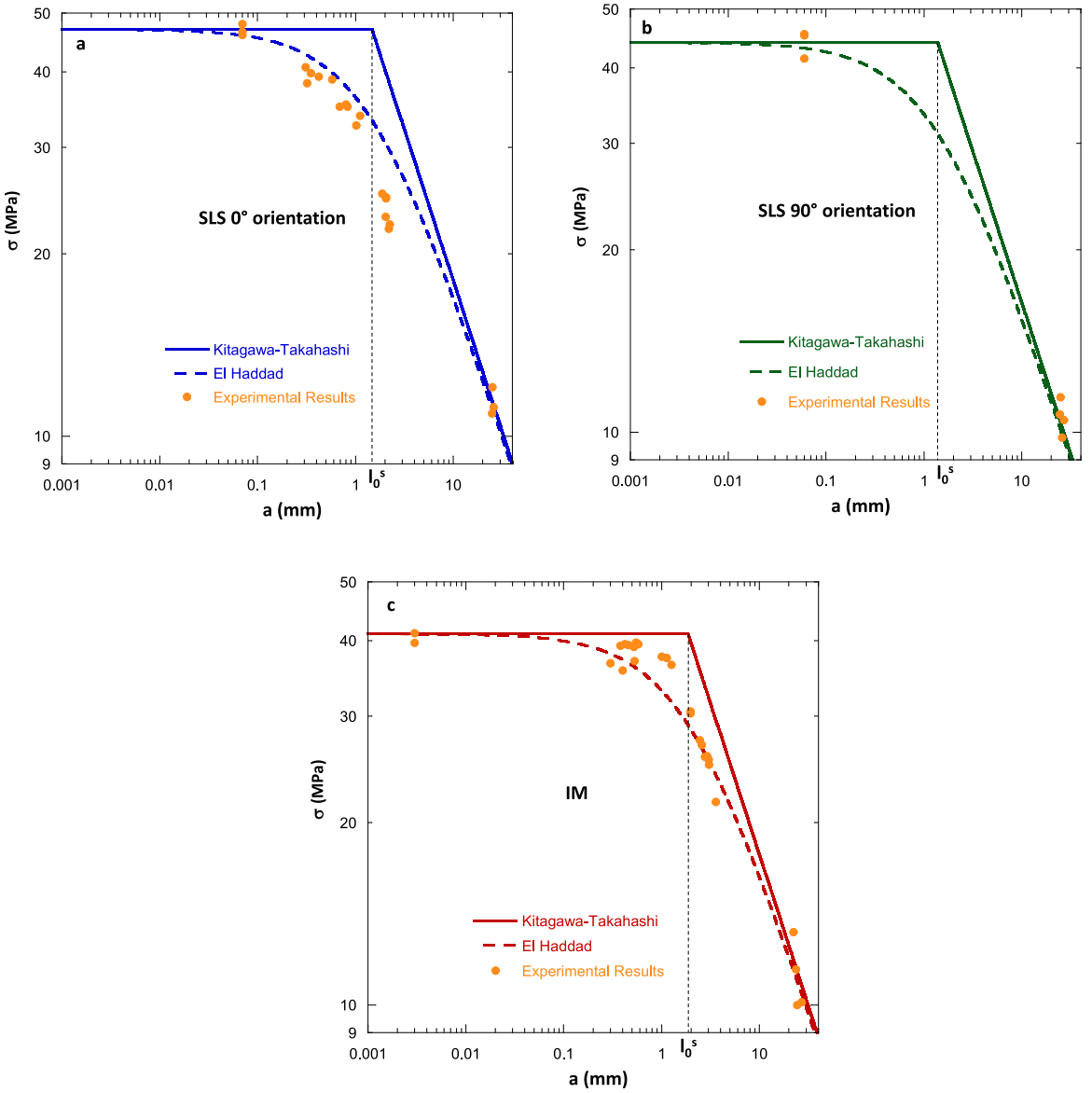

Fig. 12. Residual strength diagrams including modified Kitagawa-Takahashi (continuous line) and modified El Haddad (dotted line) approaches of (a) SLS PA-12 at 0° orientation, (b) SLS PA-12 at 90° orientation and (a) IM PA-12. Experimental data from tensile tests on plain samples, fracture tests on precraked samples and tests on specimens with short and medium size cracks are plotted as filled orange circles.

The results from the broad quasi-static and fatigue experimental program allowed the determination of failure diagrams or fatigue maps based on the application of the Kitagawa-Takahashi and El Haddad approaches. As expected, El Haddad equations provided more accurate predictions in the physically short crack regime. The characteristic lengths did not seem to display a trend with the manufacturing technique for either static loading conditions or "infinite" fatigue life (assuming non-failures at 10^6 cycles).

Finally, the mechanism of failure of SLS PA-12 for all testing configurations was the nucleation, growth ad coalescence of crazes, promoted by a uniform distribution of crystalline phase all along the bulk of the specimen. The very same mechanism was dominant in fracture mechanics specimens of IM PA-12 tested for fracture and fatigue crack growth characterisations, where the environment surrounding the crack tip was populated by crystalline phase. However, in case of plain samples used for the determination of tensile properties and S-N curves, where crack initiation occurred in the amorphous skin zone, the mechanism of damage was ductile tearing with necking formation and propagation along the gage length up to catastrophic rupture.

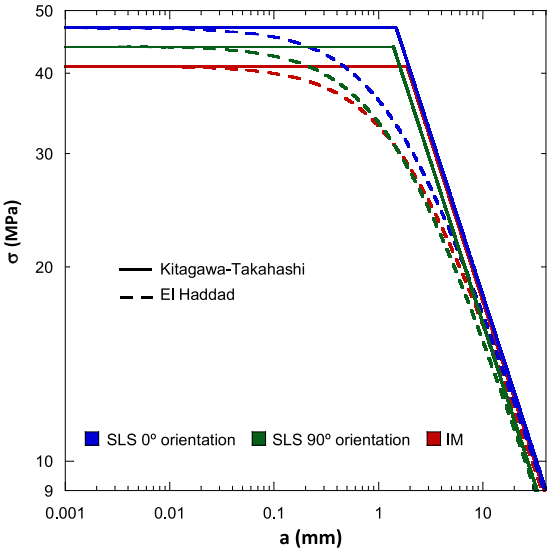

Fig. 13. Residual strength diagrams including modified Kitagawa-Takahashi (continuous line) and El Haddad (dotted line) approaches of SLS PA-12 at 0° orientation (in blue), SLS PA-12 at 90° orientation (in green) and IM PA-12 (in red).

Table 7
Static characteristic length, l_0^s, of the materials under study.

	l_0^s (mm)
SLS 0°	1.5
SLS 90°	1.4
IM	1.9

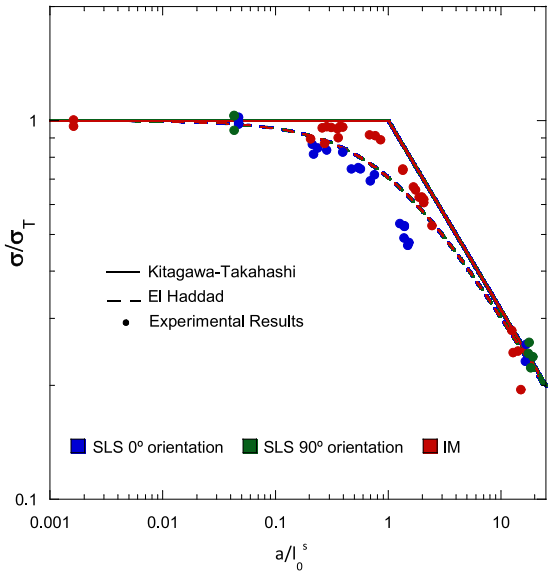

Fig. 14. Normalized residual strength diagrams including modified Kitagawa Takahashi (continuous line) and El Haddad (dotted line) approaches of SLS PA-12 at 0° orientation (in blue), SLS PA-12 at 90° orientation (in green) and IM PA-12 (in red). Experimental data from tensile tests on plain samples, fracture tests on precraked samples and tests on specimens with short and medium size cracks are plotted as filled circles.

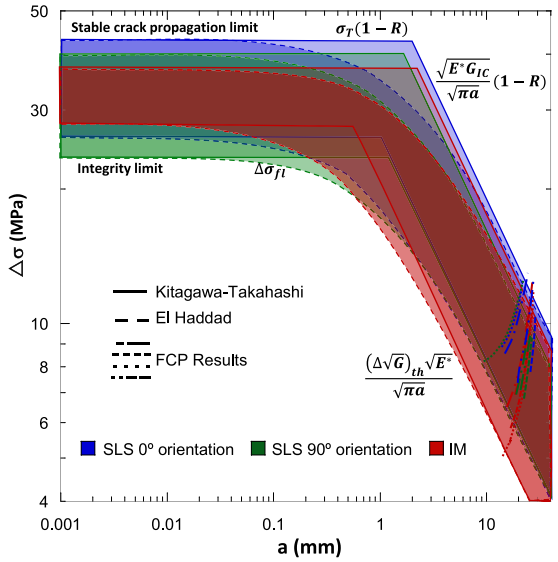

Fig. 15. Kitagawa-Takahashi diagrams (continuous line) and El Haddad approaches (dotted line) for static loading and "infinite" fatigue lifetime conditions and the fatigue crack propagation (FCP) results obtained from $\Delta\sqrt{G}$-increasing tests of SLS PA-12 at 0° orientation in blue, SLS PA-12 at 90° orientation in green and IM PA-12 in red.

CRediT authorship contribution statement

A. Salazar: Writing – review & editing, Writing – original draft, Methodology, Investigation, Funding acquisition, Conceptualization. **A.J. Cano:** Methodology, Investigation. **J. Rodríguez:** Writing – review & editing, Investigation, Funding acquisition, Conceptualization.

Declaration of Competing Interest

The authors declare that they have no known competing financial interests or personal relationships that could have appeared to influence the work reported in this paper.

Data availability

Data will be made available on request.

Acknowledgements

Authors are indebted to Ministerio de Economía y Competitividad of Spain for their financial support through project DPI2016-80389-C2-1-R.

References

[1] Kitagawa H, Takahashi S. Applicability of fracture mechanics to very small cracks or the cracks in the early stage. In: Proceedings of second international conference on mechanical behavior of materials. Metals Park: American Society for Metals; 1976. p. 627–31.
[2] Sadananda K, Vasudevan AK. Analysis of fatigue crack growth behavior in polymers using the unified approach. Mat Sci Eng A-Struct 2004;387(389):536–41. https://doi.org/10.1016/j.msea.2004.01.115.
[3] Furmanski J, Pruitt LA. Peak stress intensity dictates fatigue crack propagation in UHMWPE. Polymer 2007;48(12):3512–9. https://doi.org/10.1016/j.polymer.2007.04.006.
[4] Kanchanomai C, Thammaruechu A. Effects of stress ratio on fatigue crack growth of thermoset epoxy resin. Polym Degrad Stab 2009;94(10):1772–8. https://doi.org/10.1016/j.polymdegradstab.2009.06.012.
[5] Rans C, Alderliesten R, Benedictus R. Misinterpreting the results: how similitude can improve our understanding of fatigue delamination growth. Compos Sci Technol 2011;71(2):230–8. https://doi.org/10.1016/j.compscitech.2010.11.010.
[6] Cano AJ, Salazar A, Rodríguez J. Evaluation wof different crack driving forces for describing the fatigue crack growth behavior of PET-G. Int J Fatigue 2018;107:27–32. https://doi.org/10.1016/j.ijfatigue.2017.10.013.
[7] El Haddad MH, Topper TH, Smith KN. Prediction of non-propagating cracks. Eng Fract Mech 1979;11(3):573–84.
[8] Davidson D, Chan K, McClung R, Hudak S. Small fatigue cracks. In: Milne I, editor. Comprehensive Structural Integrity. Amsterdam: Elsevier Science; 2003. p. 129–64. https://doi.org/10.1016/B0-08-043749-4/04073-8.
[9] Chapetti M. Fatigue propagation threshold of short cracks under constant amplitude loading. Int J Fatigue 2003;25(12):1319–26. https://doi.org/10.1016/S0142-1123(03)00065-3.

[10] Atzori B, Meneghetti G, Susmel L. Material fatigue properties for assessing mechanical components weakened by notches and defects. Fatigue Fract Eng M 2005; 28(1–2):83–97. https://doi.org/10.1111/j.1460-2695.2004.00862.x.
[11] Larsen JM, Rosenberger AH, Worth BD, Li K, Maxwell DC Porter WK. Assuring reliability of gamma titanium aluminides in long-term service. In: Gamma titanium aluminides. The Materials, Metals and Minerals Society, 1999, p. 463–472.
[12] Ciavarella M, Monno F. On the possible generalizations of the Kitagawa-Takahashi diagram and of the El Haddad equation to finite life. Int J Fatigue 2006;28 (12):1826–37. https://doi.org/10.1016/j.ijfatigue.2005.12.001.
[13] Araujo JA, Nowell D. Analysis of pad size effects in fretting fatigue using short crack arrest methodologies. Int J Fatigue 1999;21(9):947–56. https://doi.org/10.1016/S0142-1123(99)00077-8.
[14] Atzori B, Lazzarin P. A three-dimensional graphical aid to analyze fatigue crack nucleation and propagation phases under fatigue limit condition. Int J Fracture 2002;118(3):271–84. https://doi.org/10.1023/A:1022965909483.
[15] Atzori B, Lazzarin P, Meneghetti G. Fracture mechanics and notch sensitivity. Fatigue Fract Eng M 2003;26(3):257–67. https://doi.org/10.1046/j.1460-2695.2003.00633.x.
[16] Rodopoulos CA, Choi JH, de los Rios ER, Yates JR. Stress ratio and the fatigue damage map. Part I. Modelling. Part II. The 2024-T351 aluminum alloy. Int J Fatigue 2004;26(7):739–46. https://doi.org/10.1016/j.ijfatigue.2003.10.017; p. 747–52. https://doi.org/10.1016/j.ijfatigue.2003.10.018.
[17] Pessard E, Bellet D, Morel F, Koutiri I. A mechanistic approach to the Kitagawa-Takahashi diagram using a multiaxial probabilistic framework. Eng Fract Mech 2013;109:89–104. https://doi.org/10.1016/j.engfracmech.2013.06.001.
[18] Sadananda K, Iyyer N. Failure Diagrams for Subcritical Crack Growth. Int J Fatigue 2022;158:106775. https://doi.org/10.1016/j.ijfatigue.2022.106775.
[19] Castellani L, Rink M. Fatigue crack growth of polymers. In: Williams JG, Moore DR, Pavan A, editors. Fracture mechanics testing methods for polymers, adhesives and composites. Oxford: Elsevier Science Ltd. and ESIS; 2001. p. 91–118.
[20] ASTM D7791-12 Standard test method for uniaxial tensile fatigue properties of plastics.
[21] Stichel T, Frick T, Laumer T, Tenner F, Hausotte T, Merklein M, et al. A Round Robin study for selective laser sintering of polymers: Back tracing of the pore morphology to the process parameters. J Mater Process Tech 2018;252:537–45. https://doi.org/10.1016/j.jmatprotec.2017.10.013.
[22] Battu AK, Pope TR, Varga T, Christ JF, Fenn MD, Rosenthal WS, et al. Build orientation dependent microstructure in polymer laser sintering: Relationship to part performance and evolution with aging. Addit Manuf 2020;36:101464. https://doi.org/10.1016/j.addma.2020.101464.
[23] Calignano F, Giuffrida F, Galati M. Effect of the build orientation on the mechanical performance of polymeric parts produced by multi jet fusion and selective laser sintering. J Manuf Process 2021;65:271–82. https://doi.org/10.1016/j.jmapro.2021.03.018.
[24] Sillani F, MacDonald E, Villela J, Schmid M, Wegener K. In-situ monitoring of powder bed fusion of polymers using laser profilometry. Addit Manuf 2022;59: 103074. https://doi.org/10.1016/j.addma.2022.103074.
[25] Beretta S, Romano S. A comparison of fatigue strength sensitivity to defects for materials manufactured by am or traditional processes. Int J Fatigue 2017;94: 178–91. https://doi.org/10.1016/j.ijfatigue.2016.06.020.
[26] Benedetti M, Santus C. Building the Kitagawa-Takahashi diagram of flawed materials and components using an optimized V-notched cylindrical specimen. Eng Fract Mech 2020;224:106810. https://doi.org/10.1016/j.engfracmech.2019.106810.
[27] Cano AJ, Salazar A, Rodríguez J. Effect of temperature on the fracture behavior of polyamide 12 and glass-filled polyamide 12 processed by selective laser sintering. Eng Fract Mech 2018;203:66–80. https://doi.org/10.1016/j.engfracmech.2018.07.035.
[28] Cano AJ, Salazar A, Rodríguez J. Effect of the orientation on the fatigue crack growth of polyamide 12 manufactured by selective laser sintering. Rapid Prototyping J 2019;25(5):820–9. https://doi.org/10.1108/RPJ-09-2018-0255.
[29] Salazar A, Cano Aragón AJ, Rodríguez J. Fatigue life assessment of polyamide 12 processed by selective laser sintering. Damage modelling according to fracture mechanics. Rapid Prototyping J 2022;28(5):814–23. https://doi.org/10.1108/RPJ-06-2021-0142.
[30] ASTM D638-03, Standard test method for tensile properties of plastics.
[31] ASTM E1820-13, Standard test method for measurement of fracture toughness.
[32] ASTM E647-13a, Standard test method for measurement of fatigue crack growth rates.
[33] Dupin S, Lame O, Barrès C, Charmeau J-Y. Microstructural origin of physical and mechanical properties of polyamide 12 processed by laser sintering. Eur Polym J 2012;48(9):1611–21. https://doi.org/10.1016/j.eurpolymj.2012.06.007.
[34] Van Hooreweder B, Moens D, Boonen R, Kruth J-P, Sas P. On the difference in material structure and fatigue properties of nylon specimens produced by injection molding and selective laser sintering. Polym Test 2013;32(5):972–81. https://doi.org/10.1016/j.polymertesting.2013.04.014.
[35] Blattmeier M, Witt G, Wortberg J, Eggert J, Toepker J. Influence of surface characteristics on fatigue behavior of laser sintered plastics. Rapid Prototyping J 2012;18(2):161–71. https://doi.org/10.1108/13552541211212140.
[36] Boukhili R, Decharentenay FX, Vu-Khanh T. Effect of frequency and orientation on fatigue crack propagation in polyamide-12. Int J Fatigue 1986;8(3):127–34. https://doi.org/10.1016/0142-1123(86)90003-4.
[37] Engel L, Klingele H, Ehrenstein GW, Schaper H. An Atlas of Polymer Damage: surface examination by scanning electron microscope. Englewood Cliffs NJ: Prentice-Hall; 1981.
[38] Raphael I, Saintier N, Robert G, Béga J, Laiarinandrasana L. On the role of the spherulitic microstructure in fatigue damage of pure polymer and glass-fiber reinforced semi-crystalline polyamide 6.6. Int J Fatigue 2019;126:44–54. https://doi.org/10.1016/j.ijfatigue.2019.04.036.
[39] Salazar A, Rico A, Rodríguez S, Navarro JM, Rodríguez J. Relating fracture behaviour to spherulite size in controlled-rheology polypropylenes. Polym Eng Sci 2012;52(4):805–13. https://doi.org/10.1002/pen.22145.
[40] Hale GE, Ramsteiner F. A testing protocol for conducting J-crack growth resistance curve tests on plastics. In: Williams JG, Moore DR, Pavan A, editors. Fracture mechanics testing methods for polymers, adhesives and composites. Oxford: Elsevier Science Ltd. and ESIS; 2001. p. 140–58.
[41] Hénaff G, Gloanec AL. Fatigue properties of TiAl alloys. Intermetallics 2005;13(5):543–58. https://doi.org/10.1016/j.intermet.2004.09.007.